Eur. Phys. J. A (2024) 60:199
https://doi.org/10.1140/epja/s10050-024-01404-5

THE EUROPEAN PHYSICAL JOURNAL A

Regular Article - Experimental Physics

Production and measurement of a stellar neutron spectrum at 30 keV

Javier Praena[1,a], **Antònia Verdera**[1], **Javier García López**[2,3], **Guido Martín-Hernández**[4]

[1] Dpto. Física Atómica, Molecular y Nuclear, Universidad de Granada, Granada, Spain
[2] Dpto. Física Atómica, Molecular y Nuclear, Universidad de Sevilla, Seville, Spain
[3] Centro Nacional de Aceleradores (Universidad de Sevilla, Junta de Andalucía, CSIC), Seville, Spain
[4] Centro de Aplicaciones Tecnológicas y Desarrollo Nuclear, 5ta y 30, Playa, La Habana, Cuba

Received: 4 March 2024 / Accepted: 19 August 2024

Communicated by Jose Benlliure

Abstract A few years ago, we theoretically studied the production of a stellar neutron spectrum at kT = 30 keV using a shaped proton beam impinging on a thick lithium target. Here, we first measure the proton distribution to better control the produced neutron spectrum. Then, we measure the forward-emitted angle-integrated neutron spectrum of the ^{7}Li(p,n)^{7}Be reaction via time-of-flight neutron spectrometry with such proton distribution. The result resembles a stellar neutron spectrum at kT = 30 keV. This method avoids in activation experiments the need for spectrum correction. In the case of spherical samples, no knowledge of the cross-section of the isotope being measured by activation would be necessary. Therefore, the present method is of interest for isotopes with unknown or poorly known cross-sections, such as branching points in astrophysics. The key point of our method is the experimental control of the proton distribution that impinges on the lithium target.

1 Introduction

One of the most interesting topics in nuclear astrophysics is the nucleosynthesis of elements beyond iron, primarily produced through successive neutron-capture reactions and beta decays [1, 2]. Neutron capture cross-section data are fundamental for calculating stellar reaction rates and reproducing the observed abundance of elements in the Universe [3]. Since neutron velocities follow a Maxwell–Boltzmann probability distribution, the neutron capture cross-section in a stellar environment is known as the Maxwellian-Averaged Cross Section (MACS), defined as

$$MACS \equiv \frac{\langle \sigma v \rangle}{v_T} = \frac{2}{\sqrt{\pi}} \bullet \frac{\int_0^\infty \sigma(E) \bullet E \bullet e^{\frac{-E}{kT}} dE}{\int_0^\infty E \bullet e^{\frac{-E}{kT}} dE} \tag{1}$$

where $\langle \sigma v \rangle$ is the reaction rate per particle pair; v_T is the particle most probable thermal velocity; and $\sigma(E)$ is the differential neutron capture cross section of the element involved as a function of the neutron energy. One of the most prolific sites for nucleosynthesis is the He-burning in red giants stars, where the typical temperature is 0.348 GK and corresponds to $kT = 30$ keV. In consequence, the MACS at $kT = 30$ keV (MACS30) are key data for stellar nucleosynthesis [4, 5].

The experimental determination of the MACS can be carried out via the time-of-flight (TOF) technique or the activation technique. The TOF technique provides the cross section as a function of the neutron energy, $\sigma(E)$, which allows calculating the MACS at several stellar temperatures. If possible, this is the best option. However, if the sample mass is significantly lower than milligrams, the TOF measurement (or differential measurement) usually lacks enough neutron fluence, and the activation technique (or integral measurement) becomes the best option due to the high flux onto the sample. Nevertheless, the activation technique is also restricted because the activation product must be radioactive or suitable for Accelerator Mass Spectrometry (AMS) measurement.

Integral measurements can directly provide the MACS at one stellar energy (kT) if the neutron spectrum irradiating the sample is a stellar spectrum. If the neutron spectrum is not stellar, a correction from the real spectrum to the stellar spectrum is needed. This correction depends on the differential cross section of the isotope for which the MACS is being measured by activation within the same energy range. Hence, it forms a 'vicious circle' because once the differential cross-section is measured or known, conducting the

[a] e-mail: jpraena@ugr.es (corresponding author)

Published online: 06 October 2024

integral measurement becomes unnecessary. Important isotopes in astrophysics lack established differential cross sections theoretical or experimental in the astrophysics energy range; consequently, the spectrum correction cannot be properly performed in many integral measurements unless the spectrum is stellar.

Stellar neutron beam production began several decades ago. In 1966, Pönitz demonstrated the feasibility of determining an absolute integral cross-section using a proton beam near the ^{7}Li(p,n)^{7}Be reaction threshold with a thick Li target. Close to the threshold (1881 keV), the neutron beam is collimated into a forward cone that can be fully covered by a sample. This allowed neutron fluence determination via ^{7}Be activity, enabling absolute integral measurements. Later, Beer and Käppeler observed that the angle-integrated neutron distribution closely approximated a Maxwellian at kT = 25 keV for a proton energy of 1912 keV.

In 1988, Ratynski and Käppeler (R&K) conducted an outstanding TOF measurement of the neutron spectrum and an integral measurement of the MACS of ^{197}Au(n,γ) at 30 keV. They demonstrated that integrating over a 70° cone aperture yielded a quasi-Maxwellian neutron spectrum at kT = 25 keV (QMNS-25), with no neutrons above 110 keV. R&K showed that the MACS30 of Au could be obtained through absolute integral measurement using the QMNS-25. However, two main corrections were necessary. The first due to differences between the true Maxwellian at kT = 25 keV and the QMNS-25. The second, for the MACS extrapolation from 25 to 30 keV. Both, spectrum correction and extrapolation, required knowledge of the differential cross-section at stellar energies. Since then, the R&K method has been widely applied to measure MACS30 for many isotopes crucial to stellar evolution and nucleosynthesis of elements.

The requirement for prior knowledge of the differential cross-section in activation experiments poses a problem for short-lived isotopes or branching points, where there is a lack of nuclear data or reliable theoretical models. To address this issue, a method to produce an exact Maxwellian or stellar neutron spectrum at 30 keV (MNS-30) was proposed [9]. With this method, the correction for the neutron spectrum is unnecessary or negligible, as well as the mentioned extrapolation, making it suitable for integral measurements on isotopes with unknown cross sections.

Test MACS30 integral measurements using simulated neutron spectra have already been conducted on stable isotopes [10, 11]. These theoretical spectra were determined using analytical descriptions of the angle-energy yield of the well-known ^{7}Li(p,n)^{7}Be reaction close to the threshold [12], and Monte Carlo (MC) simulations [13] of neutron transport through the experimental setup. Preliminary experimental data indicated that the generation of a tail in the neutron spectrum at higher energies than 120 keV could be possible [14]. Regarding the applicability of the method, challenging MACS30 integral measurements of radioactive isotopes with unknown cross sections were theoretically studied, demonstrating the method's capabilities [15].

Here, the experimental confirmation of the method for producing a stellar neutron spectrum at 30 keV is presented with a complete measurement via time-of-flight neutron spectrometry.

2 The method

Our method for producing MNS-30 is inspired by R&K, with the key being to shape the proton beam into a distribution that, upon striking the lithium target, will produce the desired neutron spectrum. Additionally, we have demonstrated that using a combined method of analytical descriptions of the angle-energy emission from the ^{7}Li(p,n)^{7}Be reaction and MC simulations, stellar spectra ranging from kT = 30 keV to 50 keV can be produced simply by increasing the energy of the proton beam while keeping the same shaper foil, see details in [16]. Here, we focus on the experimental confirmation of the production of an MNS-30, as 30 keV is the temperature of the most prolific site for nucleosynthesis, and 30 keV is used as the reference stellar temperature for comparing MACS obtained using different techniques [17].

The key point of our method is to determine the appropriate proton distribution, which involves selecting the optimal combination of proton energy and shaper foil. The shaper is characterized by its thickness and material. In previous theoretical works, we studied carbon foil as a proton beam shaper [9, 16]; however, aluminium has proven to be the most convenient shaper and was already used in activation experiments with simulated neutron spectra [10, 11]. To estimate the optimal combination of initial proton beam energy and the shaper's thickness and material, the SRIM code can be used [18]. However, due to uncertainties in the thickness of the Al foil and potential inhomogeneities, in this method, it is mandatory to measure the proton distribution for each shaper foil.

Preliminary SRIM calculations help to find the appropriate combination to produce an MNS-30. We found that a proton beam of 3.665 MeV passing through 75-μm Al thickness was an excellent combination [10]. Under these conditions, a Guassian-like proton distribution with E_c = 1.860 MeV and FWHM = 162 keV is produced. Simulations based on the well-known angle-energy yield of the ^{7}Li(p,n)^{7}Be reaction, combined with MCNP6.2 simulations, showed that impacting a thick lithium target will generate an MNS-30 [10]. Conventionally, Al foils are provided with an uncertainty in the thickness. A variation of a few micrometres in the 75-μm Al thickness can alter the proton distribution and consequently cause a slight change in the neutron spectrum, as detailed in [10]. By directly measuring the proton distributions, these uncertainties can be mitigated, and the proton energy can be adjusted until the desired distribution is achieved. In fact, the final proton energy is selected based on the results of the measured distributions.

2.1 Measurement of proton distributions

The measurement of proton distributions and characterization of Al foil were carried out at the 3-MV Tandem Pelletron accelerator at Centro Nacional de Aceleradores, CNA, (Spain) [19]. The accelerator terminal and the 90° analyzing magnet were carefully calibrated using the 991.86 keV ^{27}Al(p,γ)^{28}Si and 2409 keV ^{24} Mg(p,p'γ)^{24} Mg resonances and the Rutherford backscattering technique. Also, the energy threshold of the ^{7}Li(p,n)^{7}Be reaction was checked.

The measurement of proton distributions produced by the proton beam passing through various points of the Al foil with a nominal thickness of 75 μm was performed at the Microbeam line at CNA. This line is equipped with micrometre slits to reduce the count rate to a few Hz in the existing detectors. Such a setup was not available at the facility where the neutron TOF experiment was conducted.

The proton beam can directly impinge onto a Surface Barrier Silicon (SBS) detector (ORTEC) located at 0°, perpendicular to the beam direction. The low count rate prevents damage to the detector and maintains its energy resolution. The setup is designed to ensure an exactly reproducible perpendicular geometry. Figure 1 shows a picture of the chamber of the Microbeam line. First, we measured the direct impact of the proton beam onto the SBS detector at several proton energies and with an AmPuCm α-source we confirmed the accelerator and SBS calibrations (see Fig. 2).

Afterwards, the Al foil was installed perpendicular to the beam and the SBS detector, and the proton spectrum downstream of the Al foil was measured. Several impact points on the Al foil were measured to study potential inhomogeneities. No significant differences were found within the resolution of the SBS detector (15 keV at these energies). As previously studied in [10], differences of 15–20 keV in the proton beam do not produce appreciable differences in the MNS-30. This provides a technical advantage in case of deviation between the experimental and nominal proton energy of the accelerator calibration or a small energy loss in a thin additional layer on top of the lithium, which occurs when lithium is irradiated by protons. The work of Lederer et al. [20], aimed at confirming the R&K method, highlighted this problem.

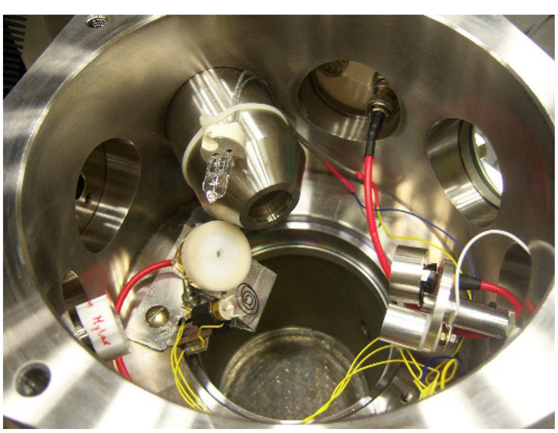

Fig. 1 Picture of the microbeam chamber at CNA

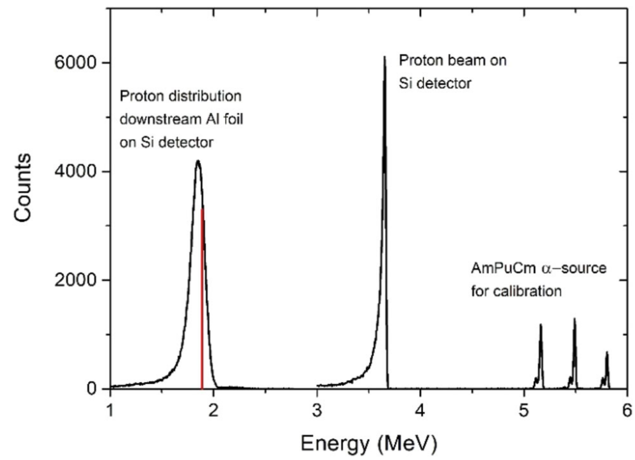

Fig. 2 Proton distributions measured at CNA. From the right to the left: spectra and α-signals from the Am-Pu-Cm source, proton beam of 3.665 MeV impinging directly onto the Si detector, and shaped proton beam downstream the Al foil. The spectra have the conventional long tail at lower energies due to the charge collection of the detector. Red line indicates the ^{7}Li(p,n)^{7}Be reaction threshold

Figure 2 shows one of the measured proton distributions which can be fitted with a Gaussian distribution with E_c = 1.860 MeV and FWHM = 162 keV. The vertical red line indicates the ^{7}Li(p,n)^{7}Be reaction threshold.

In previous theoretical studies [9, 16], we discussed that the shaped proton distribution must monotonically decrease with energy above the threshold, and a significant fraction of protons must have energies close to 2 MeV to generate an MNS-30. Deviations from these two conditions will result in departures from a stellar spectrum at 30 keV, either in shape or in stellar energy. The recent work by Musacchio-González et al. unfortunately demonstrates the importance of these two conditions, as the neutron spectrum was generated at 28.35 keV instead of 30 keV due to the lack of proton distribution measurement [21].

Once the Al foil and the proton distribution were characterized, the same foil was used for the measurement of the MNS-30.

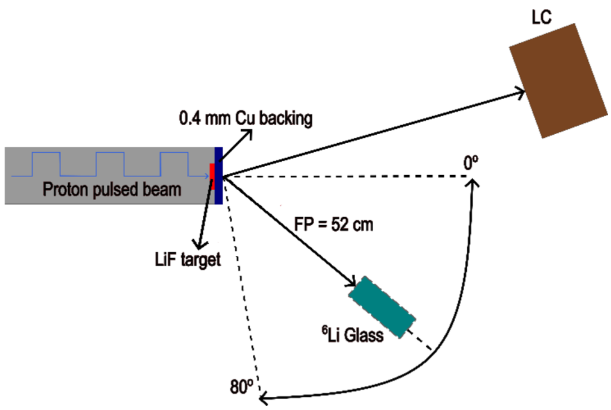

Fig. 3 Sketch of the experimental setup. The detectors were located at the beam line height. LC stands for Long Counter detector and the flight path was 52 cm

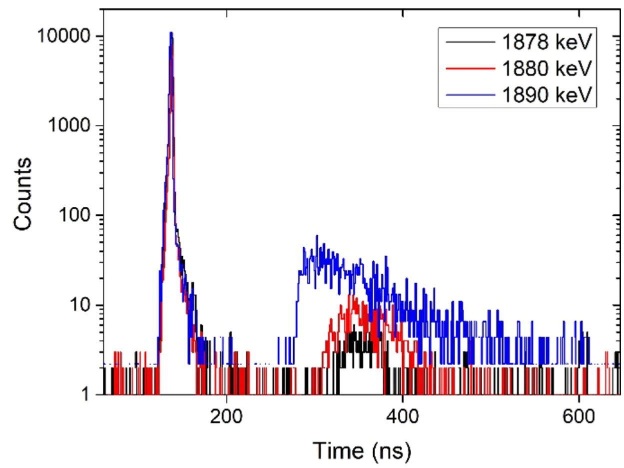

Fig. 4 Time histograms acquired with the ^{6}Li-glass detector at 0° for three proton energies close to the reaction threshold. First peak corresponds to prompt gammas or gamma-flash that is used as time zero. Second peaks correspond to the neutrons

3 Neutron spectra measurement

The experiment for determining the neutron spectrum was performed at the 7-MV Van de Graaff laboratory at IRMM (Belgium) [22]. The accelerator terminal was calibrated using the 991.86 keV ^{27}Al(p,γ)^{28}Si and 2409 keV ^{24}Mg(p,p'γ)^{24} Mg resonances The 90° analyzing magnet was calibrated with NMR probe. The accelerator was operated in pulsed mode with a frequency of 625 kHz for TOF measurements. The pulse width was 2-ns FWHM.

The proton beam (4-mm diameter) passed through a 5-mm diameter collimator before crossing the Al foil when it was installed. The target assembly consisted of an aluminium cylinder (4.2-cm diameter and 15-cm long) and 0.4-mm thick copper backing for the lithium target. LiF thick target (6-mm diameter and 90 mg) was prepared by evaporation onto Cu backing. The target assembly was cooled by a forced air flow on the external side of the Cu backing which sustained the vacuum. Figure 3 shows a sketch of the setup. Two ^{6}Li-glass detectors (5.08-cm diameter and 2.54-cm thick) were used in the analysis and were located at the same height of the lithium target at a flight path of 52 cm. Long Counter was used as monitoring.

The acquisition was carried out from the photomultiplier of each detector; the signals were split to pulse-height and to fast-timing circuits. The latter was composed of a timing filter amplifier and a constant-fraction discriminator whereas the former consisted of a preamplifier and a spectroscopy amplifier. The timing signal from each detector provided the TOF start signal in an allocated time-to-amplitude converter (TAC). A beam pick-up monitor, placed upstream of the target, provided a signal that was processed through a timing filter amplifier and a constant fraction discriminator and provided the common TOF stop signal to the TAC. Data for every detector were acquired independently, while the timing and pulse-height information for each detector were acquired in coincidence.

3.1 TOF spectra without Al foil

The experiment began by checking the ^{7}Li(p,n)^{7}Be reaction threshold with the measurement of TOF spectra. Figure 4 shows time spectra for three proton energies. The separation between the gammas (first peak) and the neutrons (second peaks) was very good. At a proton energy of 1878 keV, neutrons were clearly detected, meanwhile no neutrons were detected at 1877 keV even the detector was located closer to the target. Therefore, an offset of 3 keV was added to the accelerator calibration because the reaction threshold is expected at 1881 keV. At first glance, the maximum neutron energy at 1890 keV corresponds to around 73 keV (141 ns), in good agreement with the kinematics of the ^{7}Li(p,n)^{7}Be reaction. Hereafter, the 3 keV offset is already considered.

Then, the accelerator was set at 1912 keV proton energy and the spectrum at 0° was acquired. The corresponding angle-integrated spectrum, or R&K spectrum, has been measured by different authors [8, 20, 23, 24]. This spectrum has been extensively used in MACS measurements where the neutron spectrum at 0° was always acquired and analysed as a further verification of the conditions of the experiment regarding proton and neutron energies.

Figure 5 shows such 0° time histogram, where the maximum energy of neutrons is around 112 keV (113 ns) in good agreement with the expected result. However, the gamma-flash width suffers of an increment compared to lower proton energies. This is related to the accelerator source, and it will be a key point of the analysis of the experiment at higher proton energies, as explained later.

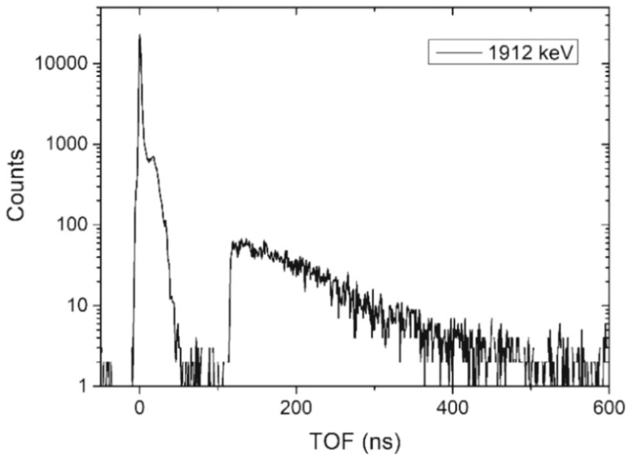

Fig. 5 Time-of-flight histogram acquired at 0° with the ^{6}Li-glass detector for 1912-keV proton energy

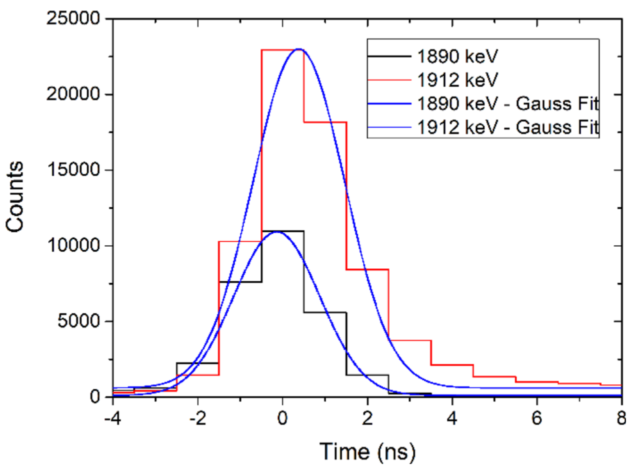

Fig. 6 Comparison of the gamma-flash at 1890 keV (Fig. 4), black line, and at 1912 keV (Fig. 5), red line. Both histograms are fitted with Gaussians, blue lines, with FWHM = 2.39 and 2.55 ns, respectively

The gamma-flash width indicates the duration in time of the proton pulses and, thus, determines the time resolution of the beam. This parameter is relevant because it plays a role in the TOF-to-energy conversion, as explained later. Figure 6 shows the comparison of the gamma-flash between 1890-keV proton energy (Fig. 4) and 1912-keV proton energy (Fig. 5). The Gaussian fit of the former provides a FWHM = 2.39 ns and FWHM = 2.55 ns for the later.

4 Data analysis

As mentioned before, to check the data analysis procedure and acquisition, we first analyse the 0° neutron spectrum produced at 1912 keV because it has been measured several times and it can be considered as a standard [20]. The data analysis of all neutron spectra of the present work are

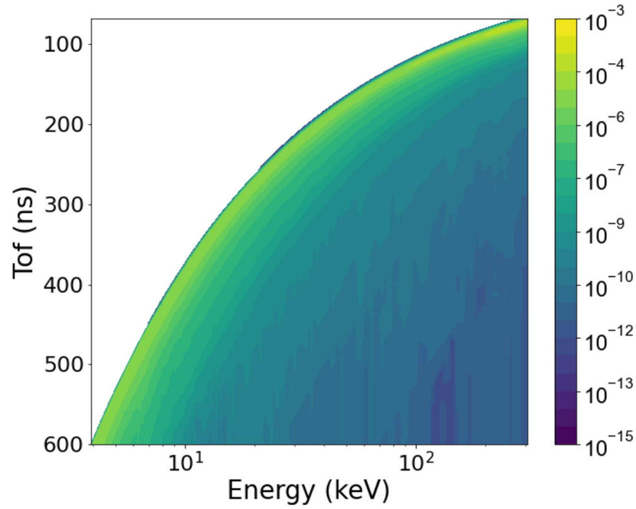

Fig. 7 Response matrix of the present experiment

determined by the TOF-to-energy conversion. As it has been pointed out in a previous work where the R&K spectrum was measured [24], the TOF for a given energy varies because the possible different paths between the production point in the target and the final point in the detector where the ^{6}Li(n,t)^{4}He reaction takes place. In this path, the neutron undergoes in multiple scattering events which depend on its energy and the materials it passes through. Consequently, for a single neutron energy the resulting TOF is a distribution. Therefore, the conversion TOF-to-energy is characteristic of each setup. Unfortunately, the conversion cannot be measured directly in neutron TOF experiments, thus, is conventionally obtained by means of detailed and accurate MC simulations. Hence, for a correct TOF-to-energy conversion, we carefully simulate with MCNP6.2 the complete setup. This includes to model the neutron source as time-dependent Gaussian distribution with FWHM = 2.55 ns and the geometry of the ^{6}Li-glass detectors, Fig. 7 shows the result of the simulations.

Regarding the geometry of the ^{6}Li-glass detectors, they were purchased to Scionix Ltd. (Scionix) with a sheet with detailed geometry. The works of Lederer et al. [20], Feinberg et al. [23], and Macías et al. [24] showed small contributions to the intrinsic efficiency due to neutron-induced resonances of the elements of the glass and the surrounding materials. Considering that the diagonal elements of the response matrix represent the intrinsic efficiency, Fig. 8 shows efficiency where small dips between 20 to 50 keV are related to such resonances.

Moving forward with the TOF-to-energy conversion of the TOF histogram of Fig. 5, regarding possible contaminations, the good separation of gammas and neutrons shows the presence of some scattered signals between both peaks. This background must be subtracted. A run with a shadow

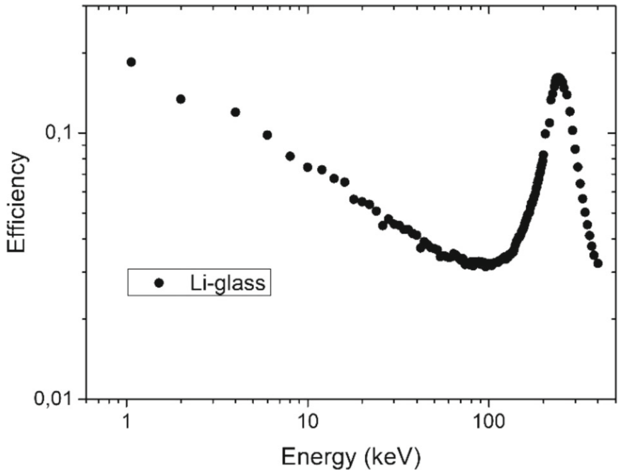

Fig. 8 Intrinsic efficiency of a ^{6}Li-glass detector (5.08-cm diameter and 2.54-cm thick)

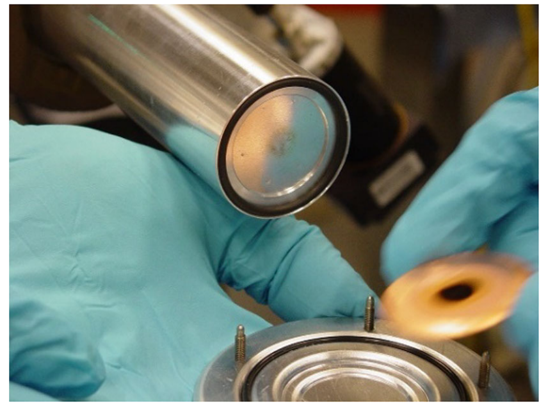

Fig. 10 Photo of the target assembly during the dismounting. Aluminium foil is located just before the LiF target. LiF is deposited onto the Cu backing

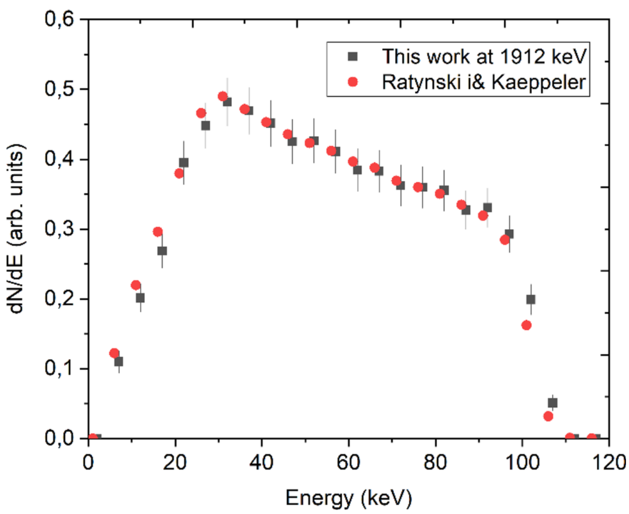

Fig. 9 Experimental neutron spectrum of this work at 0° 1912-keV proton energy (black) in comparison to the experimental data of Ratynski and Käppeler (red) [8, 20]

bar shielding the detector showed that scattered signals are due to backscattered neutrons in the experimental hall. However, this background was small and uncorrelated with the time (flat background) and can be subtracted.

The uncertainty of this measurement is mainly dominated by statistics. Therefore, once the TOF is transformed to an energy grid using the response matrix, the histograms are rebinned to 5 keV. Figure 9 shows our result in comparison to the experimental R&K neutron spectrum at 0° [8, 20]. The agreement is very good and demonstrates the feasibility of the setup introduce in the simulations, the acquisition system and the analysis procedure.

4.1 TOF spectra at higher proton energies and Al degrader

After the measurement at 0° at 1912-keV proton energy was performed, the characterized Al foil was placed close to a fresh LiF target. Figure 10 shows a photo of the target assembly during the dismounting. The Al foil was perpendicular to the target by a pushing system made of carbon fibre and located inside the target assembly. The LiF target was deposited onto the Cu backing and it became dark by proton irradiation as conventionally occurs in experiments with lithium, as mentioned before. The Cu backing acted as proton beam dump and close the vacuum by suction and its contact with a Viton O-ring. Then, the accelerator was adjusted to 3665 keV proton energy and time histograms were acquired. The protons passed through the Al foil before impacting the LiF target.

Significant differences with the time spectra at lower proton energies appeared. First, there was not separation between the gamma-flash and the neutron peak indicating a background correlated with time. Second, a double-peak structure caused the gamma-flash to appear wider, contributing to the continuity of the gamma and neutron peaks. This structure was slightly noticeable at 1912 keV (see Fig. 5, ~ 30 ns, ~ 700 counts). Third, a repetitive structure appeared at times greater than 300 ns, which was practically imperceptible at lower proton energies (see Fig. 5). Consequently, our experiment encounters a background that must be understood and properly subtracted. Figure 11 shows this background with repetitive structure after the optimization of the ion source optics (see the following explanation).

After several tests, the problem was identified. First, we explain the functioning of the chopper and buncher located at the ion source. The chopper system periodically moves the beam within its chamber, allowing the beam to pass to the buncher system only when the beam movement aligns with

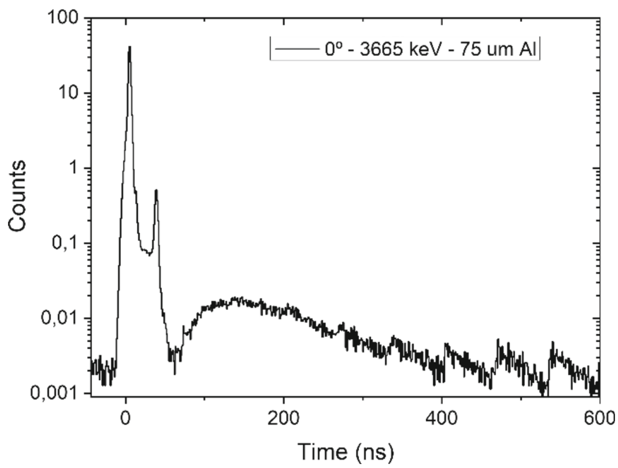

Fig. 11 Time-of-flight histogram after the optimization of the beam at the accelerator source. It was recorded by the ^{6}Li-glass detector at 0° for 3665-keV proton beam passing through the 75-µm Al foil and hitting the thick LiF target. Counts are normalized to the monitoring detector

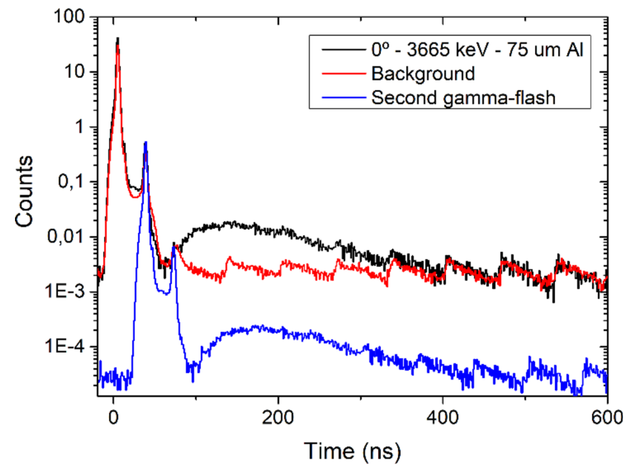

Fig. 12 Time-of-flight histogram recorded by the ^{6}Li-glass detector at 0° (black), and the two histograms to be subtracted, at angle higher than 90° (red), and the second gamma-flash and the corresponding neutrons (blue). Counts are normalized to the monitoring detector

the chopper collimator. Tests conducted without the chopper demonstrated that the repetitive structure was correlated with the buncher frequency (67 ns). This indicated that part of the proton beam was passing through the chopper collimator at any time. Since the repetitive structure was lower than the gamma-flash related to the primary proton beam, it suggested that these protons could belong to the beam's halo. In Fig. 11, the optimized proton beam shows the intensity of the repetitive structure reduced to 10,000 times lower than the primary beam.

Regarding the second peak in the gamma-flash, it was also related to the halo and possible aberrations of the optics. Therefore, by optimizing the optics of the ion source, it was possible to concentrate the broad gamma-flash into a distinct second peak (~ 30 ns), allowing for its subtraction. The repetitive structure, always present, indicated that a small halo remained between the primary and second proton peaks at the ion source. The proportion of neutrons to gammas was low, similar to the primary proton beam. Thus, just as a flat background is conventionally subtracted in such measurements, the repetitive structure can also be subtracted. To achieve this, TOF histograms were acquired at angles greater than 90°, where a negligible number of neutrons are produced. Figure 11 shows a TOF histogram after optimizing the beam at the source of the accelerator.

Once the background was understood, it could be subtracted. Figure 12 graphically illustrates the procedure, where the repetitive structure (red line) and the second gamma-flash along with the corresponding neutrons (blue line) are subtracted from the TOF histogram (black line). Figure 13 shows the result of the subtraction. It can be observed that the contribution of the second gamma-flash peak to the subtraction

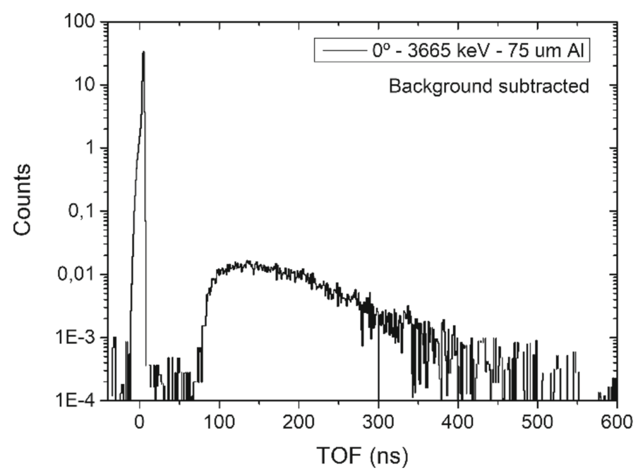

Fig. 13 Time-of-flight histogram at 0° after the background subtraction explained in the text

was lower by more than two orders of magnitude, making it practically negligible.

At first glance, Fig. 13 shows that the shape of the neutron peak at lower TOF (around 75 ns) is monotonically increasing with the time instead of a sharp shape as in the case of the TOF histogram at 0° at 1912-keV proton energy (Fig. 5). This is an indication of a tail at high neutron energies as expected for the MNS-30. Besides, the highest neutron energies are around 250 keV (75 ns) in excellent agreement with the expected MNS-30.

Returning to the point of the duration of the proton pulses, the gamma-flash resulting from the background subtraction can be fitted with a Gaussian with FWHM = 2 ns. This result may suggest a successful subtraction, as it corresponds to a value closer to the expected proton width of the experiment despite the issues with the ion source.

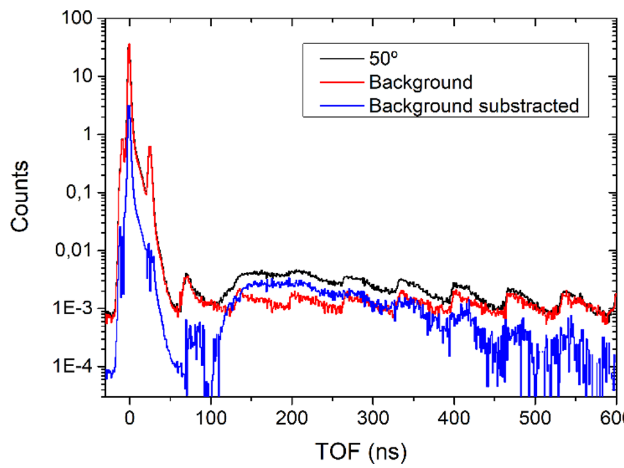

Fig. 14 Time-of-flight histogram recorded by the ^{6}Li-glass detector at 50° (black), background measured at angle higher than 90° (red), and the result of the subtraction (blue). Counts are normalized to the monitoring detector

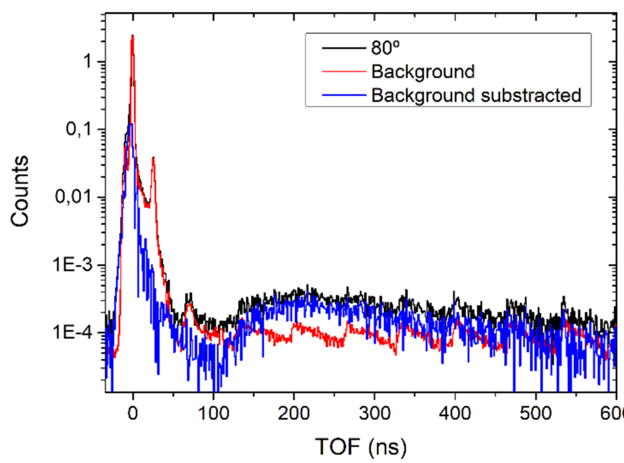

Fig. 15 Time-of-flight histogram recorded by the ^{6}Li-glass detector at 80° (black), background measured at angle higher than 90° (red), and the result of the subtraction (blue). Counts are normalized to the monitoring detector

The same subtraction procedure of the repetitive structure was applied to the rest of the measured angles, from 0° to 80° in 10° increments. It is worth mentioning that the background with a repetitive structure is an issue of the analysis, while the impact of the second gamma-flash is negligible.

For angles higher than 0°, the signal-to-background ratio was worse. Therefore, we include here the subtraction for 50° and 80°. Figure 14 shows the subtraction procedure for 50°. The resulting spectrum (blue line) was further restricted for the TOF-to-energy conversion to the range from 102 ns (135 keV) to 330 ns (13 keV) because higher TOFs are dominated by background fluctuations. Figure 15 illustrates the worst-case scenario for the signal-to-background ratio, 80°.

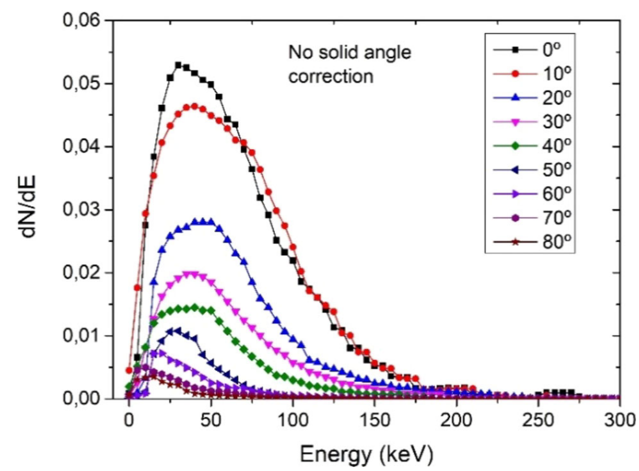

Fig. 16 Neutron spectra from 0° to 80° in steps of 10°. Spectra are not corrected for the respective solid angle

The resulting spectrum (blue line) was restricted for the TOF-to-energy conversion to the range from 118 ns (101 keV) to 360 ns (11 keV) due to dominant background fluctuations at higher TOFs. In both cases, as well as all the angles, the value of the flat background between the gamma-flash and the neutron peak, was subtracted.

Both angles, 50° and 80°, provide TOF histograms where the neutron peak at lower TOF (~ 100 ns) show a smooth increase over time, indicating a smooth decreasing tail for the fastest neutrons.

Once the TOF histograms have been cleaned of the different backgrounds, the TOF-to-energy conversion is carried out using the response matrix. Figure 16 shows the neutron spectra for each detector, normalized to the number of counts registered in the monitoring detector. The results are presented with a constant bin of 5 keV, balancing good energy resolution and reasonable statistics. With this binning the statistics uncertainty ranges from 3 to 12%, not included in the display for clarity.

To obtain the neutron spectrum at the production target, angle-integrated neutron spectra are needed. For this, each spectrum is scaled by the respective covered solid angle. For angles (α) higher than 0° the factors are calculated as,

$$f_\alpha = \cos(\alpha - 2.79°) - \cos(\alpha + 2.79°) \tag{2}$$

And for the 0° position as,

$$f_0 = 1 - \cos(2.79°) \tag{3}$$

where 2.79° is the half of the covered angle by the detector. Figure 17 shows the neutron spectra for each detector normalized to the number of counts registered in the monitoring detector and corrected by the corresponding solid angle.

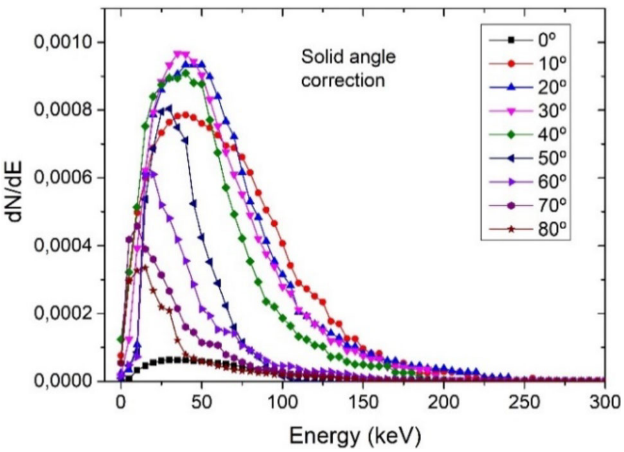

Fig. 17 Neutron spectra from 0° to 80° in steps of 10°. Spectra are corrected for the respective solid angle

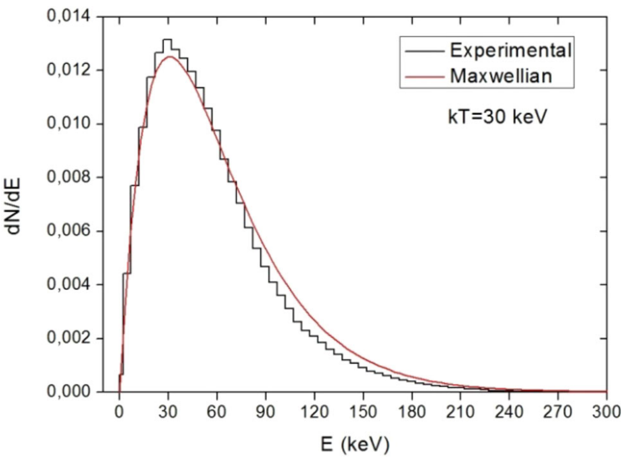

Fig. 18 Experimental neutron spectrum generated in the present work (black), Maxwellian distribution fit (red) with the normalization constant and the stellar energy as free parameters. The corresponding result is kT = 30 ± 0.3 keV

For the present setup with a flight path of 52 cm and 5.08-cm diameter detectors, the whole forward hemisphere is not covered. However, the possible differences of the angle-integrated spectrum have been studied for other authors at 1912-keV proton energy [20, 24]. They demonstrated that the possible differences are negligible. Figure 18 shows the final angle-integrated experimental spectrum obtained in the present work (black histogram). The experimental data are fitted with a Maxwellian distribution (red line),

$$f_{Max} = A \cdot E \cdot e^{-E/kT} \tag{4}$$

with the normalization constant (A) and the stellar energy (kT) as free parameters. With an orthogonal linear regression is obtained $kT = 30 \pm 0.3$ keV with $R^2 = 0.99$. The results show a very good agreement between the experimental neutron spectrum and a stellar neutron spectrum at $kT =$ 30 keV.

Regarding the quotation of uncertainties, the most significant source is statistical, as already mentioned, ranging from 3 to 12%, when selecting bins of 5 keV. Other sources are related to the simulations of the response matrix, which contribute less than 1%, and the proton width, which is already included in the response matrix simulations. The ^{6}Li(n,t)^{4}He reaction is an IAEA standard in the energy range, thus, contributing less than 2%. The dimensions of the ^{6}Li-glass are difficult to measure with high precision; however, the excellent agreement at 1912 keV in the 0° spectrum with R&K indicates that the geometry used in the simulations is correct. Therefore, for the final Maxwellian distribution, we estimate an uncertainty of 10% in the bins from 0 to 15 keV, 5% in the bins from 20 to 90 keV, and 15% for the bins above 90 keV.

5 Conclusions

The main purpose of the present work was the production and measurement of a stellar neutron spectrum at kT = 30 keV. The goal was to expand the possibilities in integral measurements of MACS at 30 keV by avoiding the spectrum correction. The spectrum correction depends on the differential cross-section of the element for which the MACS is being determined in the integral measurement. Thus, for elements with poor or unknown differential cross-section data, this correction becomes problematic and could introduce uncontrolled sources of uncertainty. Generating a stellar neutron spectrum solves this problem. Additionally, instead of generating a spectrum at 25 keV as done by R&K, we produced it at 30 keV. Thus, the extrapolation from 25 to 30 keV, which also requires knowledge of the differential cross-section, is not necessary.

Regarding possible corrections when flat samples are used, we will postpone such discussion for a forthcoming work based on the measurement of the MACS30 of ^{197}Au(n,γ) with a flat sample. Nevertheless, in case of spherical samples, no knowledge of the cross-section of the isotope being measured by activation would be necessary.

It is worth mentioning that the present technique requires the measurement and control of the energy distribution of the proton beam. This distribution must be monotonically decreasing with the energy and must have protons with energies close to 2 MeV. As it has been shown, the direct measurement of the proton beam is possible, and it is a key aspect of this method.

Regarding the time-of-flight experiment, although the present measurement suffered from significant background due to problems with the optics of the ion source of the accelerator, it has been possible to subtract it. As a result, the angle-integrated spectrum closely resembles a stellar or Maxwellian spectrum at 30 keV. Thus, the goal of the experiment has been achieved.

After the experimental confirmation of the stellar spectrum at 30 keV, we will conduct an absolute integral measurement of the MACS30 of ^{197}Au(n,γ) of interest to the IAEA [25]. This quantity is extremely important in stellar nucleosynthesis and as neutron standard [26]. The fact that differential measurements and evaluations are consistently higher than the Ratynski and Käppeler value has called their work into question [27, 28]. The measurement with the method of the present work will provide added information to improve our knowledge and potentially establish a new standard value.

Acknowledgements This work has been carried out within the framework of project PID2020.117969RB.I00 funded by MICIU/AEI/10.13039/501100011033 and the European Commission within the Seventh Framework Programme through EUFRAT (EURATOM contract no. FP7-211499). The authors thank to F.-J. Hambsch and A. Krása for the excellent support during the experiment. The authors thank to the operators of the IRMM Van de Graaff accelerator for the many extra hours they devoted trying to provide the best possible conditions for this experiment. The authors thank J.A. Labrador and A. Romero for the excellent performance of the CNA accelerator. J.P. acknowledges support and constructive discussions with F. Käppeler.

Author contribution

JP: conceptualization, preparation of experiments, data taken, simulations, analysis, writing original draft, funding acquisition. AV: simulations, analysis 1912 keV, revision of the original draft. JGL: preparation experiment CNA, data taken. GMH: conceptualization, preparation of experiments, simulations, revision of the original draft.

Data Availability Statement Data will be made available on reasonable request. [Authors' comment: The data are available from the corresponding author, J.P., upon reasonable request].

Code Availability Statement Code/software will be made available on reasonable request. [Author's comment: The sofware used to analyse the experiment is avaible from the corresponding author, J.P., upon reasonable request].

References

1. E.M. Burbidge, G.R. Burbidge, W.A. Fowler, F. Hoyle, Synthesis of elements in stars. Rev. Mod. Phys. **29**(4), 547–650 (1957). https://doi.org/10.1103/RevModPhys.29.547
2. A.G.W. Cameron, Nuclear reactions in stars and nucleogenesis. PASP **69**, 201 (1957). https://doi.org/10.1086/127051
3. Z.Y. Bao et al., Neutron cross sections for nucleosynthesis studies. Atomic Data Nucl. Data Tables **76**, 70–154 (2000). https://doi.org/10.1006/adnd.2000.0838
4. T. Rauscher, P. Mohr, I. Dillmann, R. Plag, Opportunities to constrain astrophysical reaction rates for the s-process via determination of the ground-state cross-sections. Astrophys. J. **738**, 143 (2011). https://doi.org/10.1088/0004-637X/738/2/143
5. R. Galino et al., Evolution and nucleosynthesis in low-mass asymptotic giant branch stars. II Neutron capture and the s-process. Astrophys. J. **497**, 388–403 (1998). https://doi.org/10.1086/305437
6. W. Pönitz, The (n, γ) cross section of 197Au at 30 and 64 keV neutron energy. J. Nucl. Energy Parts A/B **20**, 825–834 (1966). https://doi.org/10.1016/0368-3230(66)90117-0
7. H. Beer, F. Käppeler, Neutron capture cross sections on ^{139}Ba, ^{140,142}Ce, ^{175,176}Lu, and ^{181}Ta at 30 keV: prerequisite for investigations of the ^{176}Lu cosmic clock. Phys. Rev. C **21**(2), 534–544 (1980). https://doi.org/10.1103/PhysRevC.21.2139
8. W. Ratynski, F. Käppeler, Neutron capture cross section on ^{197}Au: a standard for stellar nucleosynthesis. Phys. Rev. C **37**, 595–604 (1988). https://doi.org/10.1103/PhysRevC.37.595
9. J. Praena, P.F. Mastinu, G. Martín-Hernández, A method to obtain a Maxwell–Boltzmann neutron spectrum at kT =30 keV for nuclear astrophysics studies. Pub. Astron. Soc. Austr. **26**, 225 (2009). https://doi.org/10.1071/AS08043
10. J. Praena et al., Measurement of the MACS of ^{181}Ta(n, γ) at kT=30 keV as a test of a method for Maxwellian neutron spectra generation. Nucl. Inst. Meth. A **727**, 1–6 (2013). https://doi.org/10.1016/j.nima.2013.05.151
11. J. Praena et al., Measurement of the MACS of ^{159}Tb(n, γ) at kT = 30 keV by activation. Nucl. Data Sheets **120**, 205–207 (2014). https://doi.org/10.1016/j.nds.2014.07.047
12. C.L. Lee, X.-L. Zhou, Thick target neutron yields for the ^{7}Li(p, n$^{)}$7Be reaction near threshold. Nucl. Instrum. Methods B **152**, 1–11 (1999). https://doi.org/10.1016/S0168-583X(99)00026-9
13. Werner CJ et al (2018) MCNP6.2 Release Notes—report LA-UR-18–20808 (Los Alamos National Laboratory (LANL).
14. P. Jiménez-Bonilla, J. Praena, J.M. Quesada, On the activation method for stellar cross-sections measurements: flat sample correction in measurements relatives to gold. NIC XV Conf Springer Proc Phys **219**, 381–384 (2018). https://doi.org/10.1007/978-3-030-13876-9_70
15. J. Praena et al., Current quests in nucleosynthesis: present and future neutron induced reaction measurements. EPJ Web Conf. **66**(07022), 1–8 (2014). https://doi.org/10.1051/epjconf/20146607022
16. G. Martín-Hernández et al., Temperature-tuned Maxwell–Boltzmann neutron spectra for kT ranging from 30 up to 50 keV for nuclear astrophysics studies. App. Rad. Isop. **70**(8), 1583–1859 (2010). https://doi.org/10.1016/j.apradiso.2012.05.004
17. KADoNiS v0.3—The third update of the "Karlsruhe Astrophysical Database of Nucleosynthesis in Stars". I. Dillmann, R. Plag, F. Käppeler, T. Rauscher. Submitted as proceeding of the workshop "EFNUDAT Fast Neutrons - scientific workshop on neutron measurements, theory & applications" held on April 28–30 2009 at Geel, Belgium.
18. J.F. Ziegler, M.D. Ziegler, J.P. Biersack, SRIM—the stopping and range of ions in matter. Nucl. Instrum. Methods Phys. Res. B **268**, 1818–1823 (2010). https://doi.org/10.1016/j.nimb.2010.02.091

19. J. García López et al., CNA: the first accelerator-based IBA facility in Spain. Nucl. Instrum. Methods Phys. Res. A **161–163**, 1137–1142 (2000). https://doi.org/10.1016/S0168-583X(99)00702-8
20. C. Lederer et al., Definition of a standard neutron field with the ^{7}Li(p, n$^{)}$7Be reaction. Phys. Rev. C **85**, 055809 (2012). https://doi.org/10.1103/PhysRevC.85.055809
21. E. Musacchio-González et al., Maxwell–Boltzmann-like neutron spectrum production for Maxwellian averaged cross sections measurements. Nucl. Inst. and Meth. A **1063**, 169255 (2024). https://doi.org/10.1016/j.nima.2024.169255
22. Sage, C. *et al.* High resolution measurements of the ^{241}Am(n,2n) reaction cross section. Phys. Rev, C 81 064604 (2010). https://doi.org/10.1103/PhysRevC.81.064604
23. G. Feinberg et al., Quasi-stellar neutrons from the ^{7}Li(p, n$^{)}$7Be reaction with an energy-broadened proton beam. Phys. Rev. C **85**, 055810 (2012). https://doi.org/10.1103/PhysRevC.85.055810
24. M. Macías, B. Fernández, J. Praena, The first neutron time-of-flight line in Spain: Commissioning and new data for the definition of a neutron standard field. Rad. Phys. and Chem. **168**, 108538 (2020). https://doi.org/10.1016/j.radphyschem.2019.108538
25. Meeting on Neutron Data Standards, 12–16 October 2020, IAEA Headquarters, Vienna, Austria. https://www-nds.iaea.org/index-meeting-crp/CM-NDS-2020-10/
26. A.D. Carlson, Work on the neutron standards since the completion of the standards evaluation. EPJ Web Conf **239**, 08001 (2020). https://doi.org/10.1051/epjconf/202023908001
27. N.V. Kornilov, V.G. Pronyaev, S.M. Grimes, Systematic distortion factor and unrecognized source of uncertainties in nuclear data measurements and evaluations. Metrology **2**, 1–18 (2022). https://doi.org/10.3390/metrology2010001
28. Pronyaev, V.G. ^{197}Au(n,γ) Standard Cross Section and Experimental Data. *Report INDC(NDS)-0540* 2009, p. 29. Available online: https://www-nds.iaea.org/standards-cm-oct-2008/9.PDF (accessed on 30 September 2022).